Computational investigation of the hexagonal honeycomb adsorption reactor for cooling applications

Giorgos Papakokkinos*, Jesús Castro, Carles Oliet, Assensi Oliva

Heat and Mass Transfer Technological Center (CTTC) Universitat Politècnica de Catalunya-BarcelonaTech (UPC)
ESEIAAT, Colom 11, E-08222 Terrassa, Barcelona, Spain

Abstract

Adsorption cooling is a sustainable technology, since it can utilize solar energy or waste heat, while employing substances without ozone depletion and global warming potential. The adsorption reactor design is determinant for the system performance. An underexplored geometry hitherto – the hexagonal honeycomb adsorption reactor – was numerically investigated. An in-house, validated, three-dimensional computational model based on unstructured meshes was employed. The Specific Cooling Power (SCP) and Coefficient of Performance (COP) were quantified for several geometrical and operational parameters. The cell inradius creates a dichotomy between SCP and COP, being 218.9 W/kg_s and 0.356 for 1 mm, while being 80.4 W/kg_s and 0.606 for 6 mm. The cell height influences prominently the SCP, being 159.5 W/kg_s and 86.1 W/kg_s for 5 mm and 30 mm, respectively. The fin thickness impacts mostly the COP, being 0.599 and 0.364 for 0.5 mm and 3 mm, respectively. Higher COP is achieved for higher evaporator, lower adsorption and lower condenser temperatures. Higher SCP is achieved for lower adsorption and condenser, and higher evaporator and desorption temperatures. Shorter cycles result in high SCP and low COP, whereas the inverse occurs for longer cycles. Aluminium heat exchanger yields 7.7% higher COP than copper. The results are discussed from a physical, as well as, an engineering perspective.

Keywords: Adsorption cooling, Adsorption packed bed reactor, Numerical simulation, Hexagonal honeycomb reactor

40-characters title suggestion (*according to the Guide for Authors*) "Honeycomb adsorption reactor for cooling"

*Corresponding author
Email address: giorgos.papakokkinos@upc.edu (Giorgos Papakokkinos)

Nomenclature

Latin characters

A	area [m^2]
a	specific exchange surface area per unit volume for spherical particles [m^{-1}]
c_p	specific heat capacity [$\mathrm{J\,kg^{-1}\,K^{-1}}$]
d_p	particle diameter [m]
D_e	effective diffusivity [$\mathrm{m^2\,s^{-1}}$]
D_0	reference diffusivity [$\mathrm{m^2\,s^{-1}}$]
E_a	activation energy [$\mathrm{J\,mol^{-1}}$]
h	specific enthalpy [$\mathrm{J\,kg^{-1}}$]
K_0	Tóth pre-exponential constant [$\mathrm{kg_w\,kg_s^{-1}\,Pa^{-1}}$]
K_D	permeability [m^2]
K_E	inertia-related parameter for Ergun equation [m]
M	mass [kg]
Nu	Nusselt number [-]
$\mathbf{n}$	surface normal vector
P	pressure [Pa]
Pr	Prandtl number [-]
$\dot{q}$	specific heat flux [$\mathrm{W\,m^{-2}}$]
q_m	Tóth monolayer capacity [$\mathrm{kg_w\,kg_s^{-1}}$]
R	universal gas constant [$\mathrm{J\,mol^{-1}\,K^{-1}}$]
R_g	gas constant [$\mathrm{J\,kg^{-1}\,K^{-1}}$]
Re	Reynolds number [-]
T	temperature [K]
t	time [s]
U_if	heat transfer coefficient at the interface between packed bed and heat exchanger [$\mathrm{W\,m^{-2}\,K^{-1}}$]
U_pi	adsorbent-adsorbate convective heat transfer coefficient [$\mathrm{W\,m^{-2}\,K^{-1}}$]
$\vec{u}$	superficial velocity vector [$\mathrm{m\,s^{-1}}$]
w	adsorbed mass [$\mathrm{kg_w\,kg_s^{-1}}$]
w^*	adsorption equilibrium capacity [$\mathrm{kg_w\,kg_s^{-1}}$]

Greek characters

α	metallic plate thickness [m]
β	cell inradius [m]
γ	cell height [m]
δ	fin thickness [m]
ΔH_{ads}	isosteric enthalpy of adsorption [$\mathrm{J\,kg^{-1}}$]
ε	void fraction [-]
λ	thermal conductivity [$\mathrm{W\,m^{-1}\,K^{-1}}$]
μ	dynamic viscosity [$\mathrm{Pa\,s}$]
ρ	density [$\mathrm{kg\,m^{-3}}$]
τ	Tóth dimensionless constant [-]

Subscripts

ad	adsorption
b	bed
con	condenser
de	desorption
eva	evaporator
f	control face
g	gas
hx	heat exchanger
if	interface between heat exchanger and packed bed
l	liquid
p	particle
pc	pre-cooling
ph	pre-heating
pi	particle interface
rel	relative
s	solid
t	total
v	vapor
w	water

Abbreviations

ACS	Adsorption Cooling System
BC	Boundary Condition
COP	Coefficient of Performance
HTF	Heat Transfer Fluid
HX	Heat exchanger
PB	Packed Bed
SCP	Specific Cooling Power [$\mathrm{W\,kg^{-1}}$]
SVF	Solid Volume Fraction [%]

1. Introduction

Cooling is progressively becoming an essential component for human well-being. A recent study identified links between cooling and all 17 Sustainable Development Goals set by the United Nations [1, 2]. Cooling demand has increased significantly in the past decades and it is expected to follow this trend in the future [3]. The increasing cooling demand raises concerns with respect to its environmental impact. It is imperative to satisfy the cooling demand utilizing environmentally-benign energy sources and refrigerants. Adsorption cooling systems (ACSs) attracted research interest, since they fulfill both characteristics. Being thermally-driven, they can utilize low temperature heat sources, such as solar thermal energy and waste heat, as well as they can employ refrigerants with zero ozone depletion and global warming potentials.

Despite the potential environmental benefits of ACSs, this technology remains underdeveloped as a result of its low performance. The desired progress will arise collectively from researches that approach ACSs from various perspectives, such as the properties of the adsorption pair materials [4], the configuration and operation of the ACS [5], its integration within a wider thermal system [6], and the design of the adsorption reactor [7] - the core component of the ACS. The presented study pertains to the latter, in particular, to the design of the hexagonal honeycomb adsorption packed bed reactor – within the wider context of solar cooling and waste heat-driven cooling.

The design of the adsorption reactor is a crucial task, since its geometric configuration influences drastically its performance, as well as it creates a dichotomy between the two performance indicators, the Coefficient of Performance (COP) and the Specific Cooling Power (SCP) [8]. On the one hand, SCP is benefited when the heat exchanger has several additional extended surfaces in order to improve heat transfer and cool down effectively the reactor during adsorption. On the other hand, COP is benefited when the heat exchanger mass is minimum, so the thermal energy lost during desorption is minimized. Thus, a compromise should be reached between COP and SCP. In order to facilitate decision-making during the design process, it is

important to characterize the reactor by quantifying these performance indicators under various geometrical configurations and operating conditions.

Computational distributed-parameters models can assist significantly the design process. Thus, they have been extensively employed for a variety of research scopes within the context of adsorption reactor research [9–12]. Our previous work [13] includes an extensive literature review, focusing on the development of the computational models. The literature review of this paper focuses on the investigation of the reactor performance under different geometrical configurations and operational conditions.

With respect to the finless cylindrical reactor, Solmuş et al. [14] used a two-dimensional axisymmetric model to simulate a cylindrical reactor with a vapor passage in its center, employing the adsorption pair water-silica gel. They studied the influence of the packed bed thickness and the impact of operational parameters, such as the driving heat source and cooling temperatures, as well as the condenser and evaporator pressures. Liu and Leong [15] studied numerically the finless cylindrical reactor with annular vapor passage, employing water and zeolite 13X. They investigated how the COP and the SCP are influenced by the operating temperatures and the heat transfer fluid (HTF) velocity.

Regarding the cylindrical reactor with circular radial fins, Niazmand and Dabzadeh [16] studied the influence of fin pitch and fin length, using a two-dimensional axisymmetric model. They concluded that the incorporation of fins reduces significantly the reactor bed size, at the cost of a slightly lower COP. Saha et al. [11] investigated numerically the same reactor geometry. They studied the impact of the cycle time and driving temperature on the performance of the system in terms of cooling capacity and COP, employing two different adsorbents. For the same geometry, Hong et al. [17] studied the effect of several parameters, concluding that the driving temperature has the strongest influence on the SCP. Khanam et al. [18] presented a study of the cycle time influence on the performance of the system, using a computational model based on ANSYS Fluent software. They reported that the SCP exhibits a maximum at cycle time of 800s, whereas COP increases as a function of the cycle time. Elsheniti et al. [19] presented a two-dimensional axisymmetric model based on COMSOL software, for the simulation of a finned tube reactor. According to their findings, they proposed smaller fin height and larger fin number, shorter desorption time by a factor of 0.7-0.9 with respect to the adsorption time, and a turbulent regime for the HTF. Mitra et al. [20] presented a two-dimensional model based on the ANSYS Fluent software. They investigated three aspect ratios of the rectangular adsorption packed bed domain, as well as two adsorbent particles size. Albaik et al. [21] utilized an in-house two-dimensional model based on cylindrical coordinates, in order to study the same geometry, concluding that the performance of the system is benefited at lower fin spacing and lower fin height.

Apart from circular radial fins, cylindrical reactors were investigated with axial (longitudinal) and square radial fins. Golparvar et al. [22] presented a three-dimensional model based on cylindrical coordinates.

The model was used for the simulation of cylindrical reactors with radial and axial fins, in a vehicular air-conditioning system driven by the exhaust gases of the engine. They studied the influence of the fin height and fin spacing on the SCP and COP. They concluded that the reactor with radial fins provides 10% higher cooling capacity than the reactor with axial fins. Mahdavikhah and Niazmand [23] studied the impact of fin pitch and fin length on the performance of a cylindrical reactor with square radial fins, using a three-dimensional model. According to their results, they emphasized the importance of these geometrical parameters on the performance of the system. Ramji et al. [24] used the ANSYS software to investigate a cylindrical adsorber reactor with axial fins, driven by exhaust heat. The influence of the wall thickness on the performance of the system was studied.

With respect to non-cylindrical geometries, Mohammed et al. [25] studied a reactor geometry consisting of two rectangular layers of packed beads separated by a vapor passage. They numerically investigated the influence of the particle diameter, bed thickness and thermal conductivity on the SCP. In a subsequent work, Mohammed et al. [26] proposed a reactor design based on rectangular modular cells. Using COMSOL software, they investigated the influence of the operating temperatures and the convective heat transfer coefficient on the SCP. Using the same software, Saleh et al. [27] investigated a wire fin heat exchanger employing aluminium fumarate as adsorbent. They concluded that the performance is improved for low fin height, fin spacing and tube diameter. Kowsari et al. [28] used a three-dimensional model for the investigation of the geometrical configuration of the trapezoidal-finned flat-tube heat exchanger. Khatibi et al. [29] used a three-dimensional model in order to investigate the geometrical parameters of the finned flat-tube heat exchanger, as well as the influence of incorporating aluminum additive particles inside the packed bed. Papakokkinos et al. [13] presented a computational model based on unstructured meshes, capable to simulate any potential geometry. Subsequently, they utilized this model to investigate the SCP of five different adsorption reactor geometries, by varying their solid volume fraction, fin thickness and fin length.

As it arises from the literature review, the vast majority of the studies focused on cylindrical reactors. This tendency results from the models' limitations, which based their spatial discretization on cylindrical coordinates. Hence, the geometric configurations which cannot be simulated using cylindrical discretization remain relatively underexplored. An example of such underexplored geometry is the hexagonal honeycomb – a bioinspired geometry that mimics the way bees build their hives [30]. This structure attracted interest since the antiquity and in 1999, the honeycomb conjecture was proven mathematically. The latter states that this hexagonal tiling is the partition of the plane in regions of equal area with the minimum perimeter [31]. From an adsorption reactor perspective, this can be interpreted as the partition of a planar reactor that requires the minimum amount of fins for a given adsorbent cell size. Although the honeycomb structure is employed within various engineering contexts [32–34] – to our knowledge, a complete study and characterization for

adsorption cooling reactors has not been reported in the literature, hitherto. Within this context, three works studied partially two variants of the honeycomb reactor [13, 35, 36]. Shi et al. [35] studied this geometry using COMSOL software. Their analysis was limited to the adsorption process, evaluating the adsorption uptake for different cell geometries and HTF Reynolds numbers. Sosnowski et al. [36] studied the proposed geometry using ANSYS Fluent software, focusing on the desorption process. They reported the temperature increase and the logarithmic mean temperature difference of the HTF. In our previous work [13], the honeycomb reactor was investigated along with four other geometries using an in-house computational model. The study focused only on the adsorption process and reported results for the SCP.

Consequently, the three studies elaborating honeycomb reactors in the context of adsorption cooling are not complete. A complete investigation is attempted in this study, by quantifying both important performance indicators – the COP and SCP – for various geometrical configurations and operating parameters. An in-house, validated computational model is employed for the simulations. The model is based on three-dimensional unstructured meshes, a necessary feature for the simulation of the studied geometry. Conjugate dynamic simulations are performed for the two domains of the reactor, namely, the heat exchanger solid and the adsorption packed bed. Parallel computing and a multi-timestep approach are employed in order to reduce the computational time.

Firstly, a geometrical study is conducted with respect to the influence of the three dimensions that define the honeycomb structure – namely the cell inradius, the cell height and the fin thickness. Subsequently, the effect of the four operating temperatures is investigated. Then, the influence of the HTF heat transfer coefficient is studied. The duration of the cycle phase is investigated through the cycle adsorption percentage. Copper and aluminium are compared as heat exchanger materials. Finally, the results are discussed from an engineering perspective, elaborating practical aspects of ACSs driven by solar energy or waste heat.

2. System description

Adsorption cooling technology is based on the phenomenon of adsorption, the adhesion of gas molecules onto a solid surface. An ACS is composed by three basic components: the adsorption reactor, the evaporator and the condenser. The adsorption thermodynamic cooling cycle is divided into four phases (a) pre-cooling, (b) adsorption, (c) pre-heating and (d) desorption. The desired cooling production is produced only in the adsorption phase. Thus, it is a common strategy to include two reactors, operating alternately, in order to avoid intermittent cooling production. While one reactor undergoes the phases a-b-c-d, the other undergoes c-d-a-b. Figure 1 depicts the ACS and Figure 2 shows the Clapeyron diagram of the ideal thermodynamic cycle. The latter is defined by the temperature of three secondary circuits T_{high}, T_{med} and T_{low}, which

deliver the HTF to the components in order to regulate their temperature. The pressure in the condenser and the evaporator correspond to the saturation pressure at their respective temperatures.

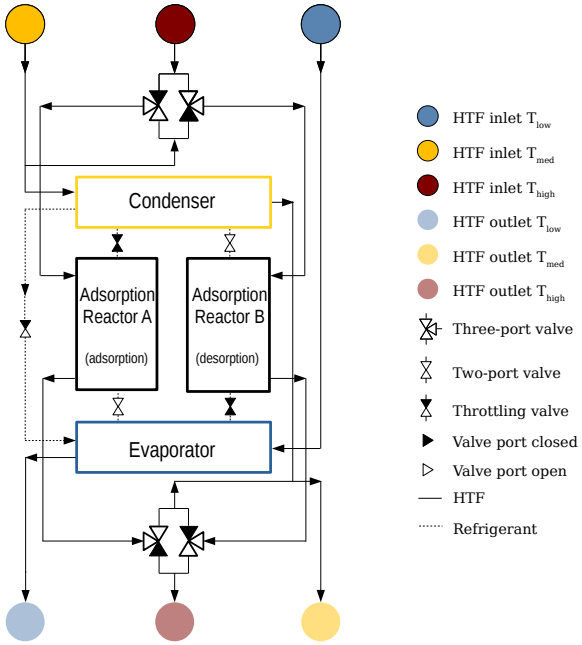

Figure 1: Schematic diagram of the ACS - Valve openings reflect the case where Adsorption Reactor A undergoes the adsorption phase while Adsorption Reactor B the desorption phase

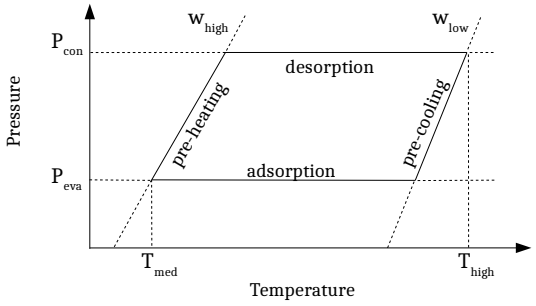

Figure 2: Clapeyron diagram for the ideal thermodynamic adsorption cooling cycle

During the adsorption phase, liquid evaporates inside the evaporator and flows towards the reactor, where it is adsorbed on the adsorbent. As a result of the exothermic nature of adsorption, the temperature of the reactor increases. This effect is disadvantageous, since the adsorption capacity decreases at higher temperature, and consequently, the cooling production is reduced. Hence, the secondary circuit delivers HTF at T_{med} in order to maintain the reactor temperature low. This task is hindered by the low heat transfer of the packed bed. Thus, the necessity of enhancing the heat transfer rate arises, and the most

common method to achieve it is by incorporating additional fins on the heat exchanger.

During the pre-heating and desorption phases, the HTF is switched to T_{high}. This heating is the energy input of the ACS, thus, it is beneficial to maintain it low. The useful thermal energy input is the amount associated to the temperature increase of the adsorbent and the endothermic sorption enthalpy. However, a part of the provided thermal energy is used for the temperature increase of the heat exchanger solid - the metal which intervenes between the HTF and the adsorbent. This amount of thermal energy is lost in every cycle – therefore, it is desired to minimize the mass of the heat exchanger.

From the above analysis it becomes evident that the reactor design determines its performance, as well as it establishes a dichotomy between the SCP and the COP. The SCP is favored by incorporating additional fins that enhance heat transfer, whereas the COP is benefited when the heat exchanger mass is kept at minimum. Consequently, a conflict arises between the SCP and the COP. The presented computational model allows to study the reactor geometry and quantify the SCP and COP under several geometrical configurations and operational conditions. As discussed in Section 5.5, the prioritization of the SCP and COP depends on the overall context of the cooling application.

3. Computational model

3.1. Introduction

The computational model for the adsorption reactor consists of two domains, the adsorption packed bed and the heat exchanger solid. The two domains are coupled by exchanging thermal energy. The assumptions adopted in the model construction are: (i) the shape and size of the adsorbent particles, as well as the void fraction, are assumed uniform throughout the packed bed, (ii) the adsorbent is an isotropic porous medium, thus its surface porosity is equivalent to its volume porosity, [37] (iii) the adsorbed phase specific heat capacity corresponds to the liquid phase, (iv) the HTF temperature is constant, (v) there are no heat losses to the environment, (vi) the vapor adsorbate has ideal gas behavior, and (vii) during the adsorption and desorption phase, the inlet vapor temperature and pressure are constant, corresponding to the saturation pressure of the evaporator and condenser, respectively.

3.2. Mathematical formulation

Adsorption equilibrium and kinetics

The adsorption equilibrium capacity is determined through the adsorption isotherm. In this study, the considered adsorbate and adsorbent are water and silica gel type RD [38], respectively. For this adsorption

pair, Wang et al. [39] derived experimentally the Tóth isotherm (equation 1).

$$w^*(P,T) = \frac{K_0 \exp(\Delta H_{\text{ads}}/(R_{\text{g}}T))P}{\left[1 + \left(\frac{K_0}{q_m}\exp(\Delta H_{\text{ads}}/(R_{\text{g}}T))P\right)^{\tau}\right]^{1/\tau}} \tag{1}$$

For the adsorption kinetics , the Linear Driving Force (LDF) model is employed [40]. For spherical particles, it is expressed as:

$$\frac{dw}{dt} = \frac{60 D_e}{d_{\text{p}}^2}(w^* - w) \tag{2}$$

The D_e is the effective diffusivity, calculated by the Arrhenius equation, based on the temperature, the reference diffusivity D_0 and the activation energy E_a.

$$D_e = D_0 \exp(-E_a/(RT)) \tag{3}$$

Mass conservation equation

The vapor density throughout the packed bed domain varies as a result of vapor fluxes and sorption phenomena. Its transient evolution is mathematically described by the mass conservation equation.

$$\varepsilon_{\text{b}}\frac{\partial \rho_{\text{g}}}{\partial t} + \nabla \cdot (\rho_{\text{g}}\vec{u}) + \rho_{\text{s}}(1-\varepsilon_{\text{t}})\frac{\partial w}{\partial t} = 0 \tag{4}$$

The total void fraction ε_{t} is a function of the bed void fraction ε_{b} and the particle porosity ε_{p} – calculated as: $\varepsilon_{\text{t}} = \varepsilon_{\text{b}} + (1-\varepsilon_{\text{b}})\varepsilon_{\text{p}}$. The mass of the gas inside a control volume dV is calculated as $\varepsilon_{\text{b}}\rho_{\text{g}}\text{dV}$, while the solid mass is calculated as $\rho_{\text{s}}(1-\varepsilon_{\text{t}})\text{dV}$.

Energy conservation equations

The local thermal nonequilibrium (LTNE) approach is adopted for the mathematical description of the heat transfer inside the packed bed. It consists in solving two individual energy conservation equations, for the solid and the gas phase. For a detailed derivation of the equations and an explanation of each term, the reader is referred to [8].

$$\text{solid: } \rho_{\text{s}}(1-\varepsilon_{\text{t}})c_{p_{\text{s}}}\frac{\partial T_{\text{s}}}{\partial t} = (1-\varepsilon_{\text{b}})\lambda_{\text{s}}\nabla^2 T_{\text{g}} + aU_{\text{pi}}(T_{\text{g}} - T_{\text{s}}) + \rho_{\text{s}}(1-\varepsilon_{\text{t}})\frac{\partial w}{\partial t}\left[\Delta H_{\text{ads}} + c_{p_{\text{g}}}(T_{\text{g}} - T_{\text{s}})\right] \tag{5}$$

$$\text{gas: } \varepsilon_{\text{b}}\frac{\partial(\rho_{\text{g}}h_{\text{g}})}{\partial t} + \nabla \cdot (\rho_{\text{g}}\vec{u}h_{\text{g}}) = \varepsilon_{\text{b}}\lambda_{\text{g}}\nabla^2 T_{\text{g}} + aU_{\text{pi}}(T_{\text{s}} - T_{\text{g}}) - \rho_{\text{s}}(1-\varepsilon_{\text{t}})\frac{\partial w}{\partial t}h_{\text{g}} \tag{6}$$

The specific heat capacity of the solid phase is evaluated taking into consideration the effect of the adsorbed mass as $(c_{p_{\text{s}}})_{\text{dry}} + w \times c_{p_{\text{l}}}$. The specific exchange surface area per unit volume a for a bed of spherical particles is calculated by equation 7 [37]. The heat transfer coefficient between the two phases U_{pi} is determined through the Nusselt number, as in equation 8 [41].

$$a = 6(1-\varepsilon_{\text{b}})/d_{\text{p}} \tag{7}$$

$$\mathrm{Nu} = 2 + 1.1\mathrm{Pr}^{0.33}\mathrm{Re}^{0.6} = \frac{U_{\mathrm{pi}} d_{\mathrm{p}}}{\lambda_{\mathrm{g}}} \tag{8}$$

The heat transfer inside the solid heat exchanger domain is described by the heat conduction equation.

$$\rho_{\mathrm{hx}} c_{p_{\mathrm{hx}}} \frac{\partial T_{\mathrm{hx}}}{\partial t} = \lambda_{\mathrm{hx}} \nabla^2 T_{\mathrm{hx}} \tag{9}$$

Pressure equation

The pressure of the water vapor is calculated based on the ideal gas law (equation 10). A comparative study was undertaken between the ideal gas law and the methodology of the International Association for the Properties of Water and Steam [42], revealing an acceptable accuracy, taking into account the drastically lower computational cost of the ideal gas law [8].

$$P = \rho_{\mathrm{g}} R_{\mathrm{g}} T_{\mathrm{g}} \tag{10}$$

Momentum equation

The Ergun equation – an extension of the Darcy equation – is employed for the calculation of momentum in porous media [37, 43].

$$\vec{u} + \frac{\rho_{\mathrm{g}}}{\mu} K_E \vec{u} |\vec{u}| = -\frac{K_D}{\mu} \nabla P \tag{11}$$

Where permeability K_D and Ergun inertia-related parameter K_E are calculated as:

$$K_D = \frac{d_{\mathrm{p}}^2 \varepsilon_{\mathrm{b}}^3}{150(1-\varepsilon_{\mathrm{b}})^2} \text{ and } K_E = \frac{1.75 d_{\mathrm{p}}}{150(1-\varepsilon_{\mathrm{b}})} \tag{12}$$

Boundary conditions

Numerical simulations require the definition of the boundary conditions (BCs) of the two domains. Figure 5 in Section 4.3 illustrates the relevant boundaries for the reactor under consideration in this study.

On the interface between the HTF and the heat exchanger solid, the boundary condition is expressed as:

$$\lambda_{\mathrm{hx}} \frac{\partial T_{\mathrm{hx}}}{\partial \mathbf{n}} = U_{\mathrm{HTF}} (T_{\mathrm{HTF}} - T_{\mathrm{hx}}) \tag{13}$$

On the vapor inlet, for the switching phases, a Neumann BC is imposed for the pressure and the two temperatures (equation 14). During adsorption and desorption, the BCs are expressed by equations 15(a-c). For the pressure, a Dirichlet BC is imposed, according to the P_{eva} and P_{con}, respectively. The gas temperature on this boundary depends on the vapor flow direction. If the flow is inwards, the gas temperature takes the value of the inlet vapor. If the flow is outwards, Neumann BC is applied. The vapor density is

calculated by the ideal gas law, based on local temperature and pressure. The natural convection between the heat exchanger solid and the vapor chamber is neglected and Neumann BC is applied (equation 16).

$$\frac{\partial P}{\partial \mathbf{n}} = \frac{\partial T_{\mathrm{g}}}{\partial \mathbf{n}} = \frac{\partial T_{\mathrm{s}}}{\partial \mathbf{n}} = 0 \tag{14}$$

$$P \ : \ \begin{cases} P = P_{\mathrm{eva}} \text{ for adsorption} \\ P = P_{\mathrm{con}} \text{ for desorption} \end{cases} \tag{15a}$$

$$T_{\mathrm{g}} \ : \ \begin{cases} T_{\mathrm{g}} = T_{\mathrm{eva/con}} & \text{when } \dot{m} \text{ is inwards} \\ \dfrac{\partial T_{\mathrm{g}}}{\partial \mathbf{n}} = 0 & \text{when } \dot{m} \text{ is outwards} \end{cases} \tag{15b}$$

$$T_{\mathrm{s}} \ : \ \frac{\partial T_{\mathrm{s}}}{\partial \mathbf{n}} = 0 \tag{15c}$$

$$\frac{\partial T_{\mathrm{hx}}}{\partial \mathbf{n}} = 0 \tag{16}$$

On the boundaries where geometrical symmetry applies, Neumann BC is imposed for all variables.

$$\frac{\partial P}{\partial \mathbf{n}} = \frac{\partial T_{\mathrm{g}}}{\partial \mathbf{n}} = \frac{\partial T_{\mathrm{s}}}{\partial \mathbf{n}} = \frac{\partial T_{\mathrm{hx}}}{\partial \mathbf{n}} = 0 \tag{17}$$

The thermal energy exchanged on the interface between the packed bed and the heat exchanger solid is evaluated by equation 18. For an extensive discussion regarding this BC, the reader is referred to [8, 13].

$$\dot{q} = U_{\mathrm{if}}(T_{\mathrm{hx,cf}} - T_{\mathrm{s,cf}}) \tag{18}$$

3.3. Numerical solution

The equations constituting the mathematical formulation presented above are numerically solved by discretizing them in space and time. An Euler implicit scheme is adopted for the temporal terms, along with a multi-timestep approach. The latter allows to reduce significantly the computational time of the simulations, without compromising the accuracy. The domains are discretized onto three-dimensional unstructured meshes, using the control volume method. Second order central difference and upwind schemes are applied for the diffusive and the convective terms, respectively. The computational model is parallelized in various CPUs, in order to reduce the computational cost. A detailed description of the numerical solution - regarding the overall algorithm, the individual solvers and the multi-timestep approach - can be found in [8].

3.4. Verification assessments and experimental validation of the model

The reliability of the numerical model was evaluated through verification assessments and experimental validation. The former pertains to studies that ensure the model consistency; namely (i) mass conservation, (ii) energy conservation, (iii) mesh independence, (iv) timestep independence, (v) adequacy of the convergence

criteria involved in the iterative procedures and (vi) correct programming implementation with respect to CPUs parallelization and memory leakage. These verification assessments are extensively presented in [8].

Moreover, the numerical results were compared to the experimental results of Jribi et al. [44], regarding a tubular finned reactor using ethanol and activated carbon as adsorption pair. The experimental validation of the model is based on the temporal evolution of the temperature in four points within the packed bed, since this approach challenges the distributed-parameter character of the model. A thorough discussion with respect to the experimental validation can be found in [8].

4. Parametric study of the hexagonal honeycomb adsorption reactor

This section details the context of the simulations, whose results are presented and discussed in Section 5.

4.1. Definition of cycle phases duration

The entire thermodynamic cycle is simulated, namely the four phases (a) pre-cooling, (b) adsorption, (c) pre-heating and (d) desorption. The cycle simulation is repeated until cyclic behavior is attained and the influence of the initial conditions is eliminated. The cycle scheme presented below was employed.

The pre-cooling duration t_{pc} is terminated when the maximum pressure inside the reactor becomes lower than the P_{eva}. The adsorption duration t_{ad} is defined by the adsorbed mass with respect to the theoretical capacity that would result if equilibrium is achieved. The minimum theoretical capacity of the cycle w^*_{min} corresponds to (P_{con}, T_{des}), while the maximum w^*_{max} to (P_{eva}, T_{ads}). The adsorbed mass across the packed bed is averaged $\overline{w}$, and its relative value with respect to ($w^*_{\mathrm{max}} - w^*_{\mathrm{min}}$) is calculated based on equation 19. The cycle adsorption percentage is the $\overline{w}_{\mathrm{rel}}$ that determines the duration of the adsorption phase. It is set to 70 % for all simulations, except in Section 5.3, where a parametric study of this value is conducted.

$$\overline{w}_{\mathrm{rel}} = \frac{\overline{w} - w^*_{\mathrm{min}}}{w^*_{\mathrm{max}} - w^*_{\mathrm{min}}} \times 100\% \tag{19}$$

Similarly to the pre-cooling phase, the pre-heating duration t_{ph} is terminated when the minimum pressure in the packed bed is higher than the P_{con}. The desorption duration t_{de} is calculated as in equation 20.

$$t_{\mathrm{de}} = t_{\mathrm{pc}} + t_{\mathrm{ad}} - t_{\mathrm{ph}} \tag{20}$$

4.2. Performance indicators

The performance indicators used for the evaluation of the reactor performance are the Coefficient of Performance (COP) and the average Specific Cooling Power (SCP). The COP is a non-dimensional parameter

comparing the useful cooling production to the thermal energy consumption of the ACS.

$$\mathrm{COP} = \frac{Q_{\mathrm{cooling}}}{Q_{\mathrm{heating}}} \tag{21}$$

where Q_{cooling} is the useful cooling produced, calculated as the product of the adsorbed mass and $\Delta H'_{\mathrm{evap}}$ (equation 23), while Q_{heating} is the thermal energy input at T_{high} during pre-heating and desorption. The SCP is the average cooling power normalized per unit of mass of adsorbent and it is measured in Wkg^{-1}.

$$\mathrm{SCP} = \frac{Q_{\mathrm{cooling}}}{M_s \times t_{\mathrm{cycle}}} = \frac{\Delta m \times \Delta H'_{\mathrm{evap}}}{M_s \times t_{\mathrm{cycle}}} = \frac{\Delta w \times \Delta H'_{\mathrm{evap}}}{t_{\mathrm{cycle}}} \tag{22}$$

where Δm is the total mass adsorbed during the adsorption phase and desorbed during the desorption phase, M_s is the dry solid adsorbent mass, and Δw is the quotient of the two aforementioned values. The cooling produced associated with Δw is denoted as $\Delta H'_{\mathrm{evap}}$ and it is calculated as:

$$\Delta H'_{\mathrm{evap}} = h_{\mathrm{v,sat}}\big|_{T_{\mathrm{eva}}} - h_{\mathrm{l,sat}}\big|_{T_{\mathrm{con}}} \tag{23}$$

where $h_{\mathrm{v,sat}}\big|_{T_{\mathrm{eva}}}$ is the enthalpy of the saturated vapor at T_{eva}, and $h_{\mathrm{l,sat}}\big|_{T_{\mathrm{con}}}$ is the enthalpy of the saturated liquid leaving the condenser, and thus, the enthalpy of the vapor-liquid mixture entering the evaporator (assuming isenthalpic expansion).

4.3. Geometrical considerations for the simulated geometry

This work investigates the hexagonal honeycomb adsorption reactor. Figure 3 illustrates a front view and a three-dimensional view of the reactor, as well as a cross-section of the vertical plane. The HTF passes through a rectangular channel. Metallic hexagonal honeycomb structures are embedded on two of the plates which form the aforementioned rectangular channel. The adsorbent is placed inside the hexagonal cells. This module is enclosed within the vapor chamber. The vapor flowing from or to the evaporator and the condenser passes through the vapor chamber. Multiple modules can be incorporated within the vapor chamber.

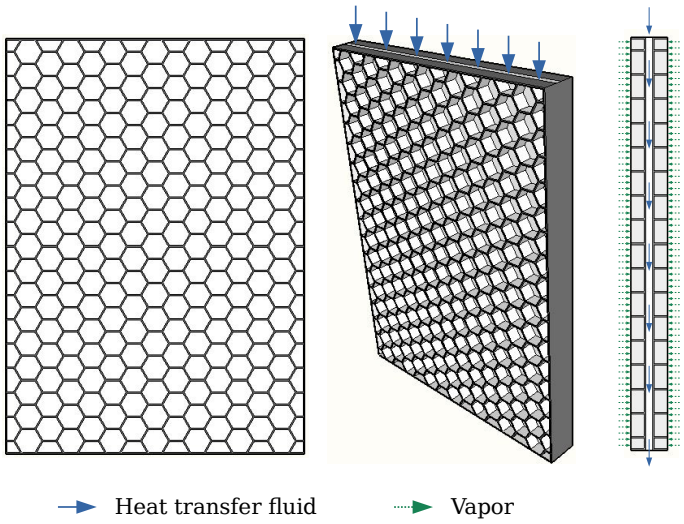

Figure 3: Front view, three-dimensional view and vertical cross-section of the hexagonal honeycomb adsorption reactor

Detailed distributed-parameter models have considerable computational consumption. Therefore, simulating the entire reactor would have unpractical computational cost. Thus, a common practice is to reduce the computational domain, taking into advantage the symmetries and the periodicities of the geometry. Assumptions (v) and (vi) (Section 3) allow to interpret the results of the reduced geometry as representative for the entire reactor. All cells are expected to behave similarly if the HTF temperature is constant across the channel, as well as if the reactor is ideally insulated. Moreover, geometric symmetry of the hexagon allows to simulate only one sixth of the cell.

Figure 4 and 5 illustrate the computational domain of the reduced geometry and its boundary conditions, respectively. The mathematical formulation of the latter was presented in Section 3.2. Figure 6 depicts the required dimensions for the definition of the hexagonal honeycomb geometry. The dimension α corresponds to the thickness of the metallic plate and it is considered as 1 mm. The three dimensions which define the geometry are the cell inradius β, the cell height γ and the fin thickness δ.

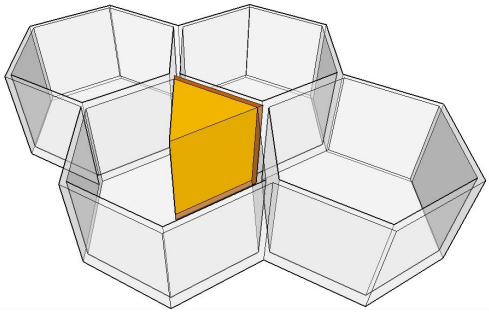

Figure 4: Computational domain of the reduced geometry

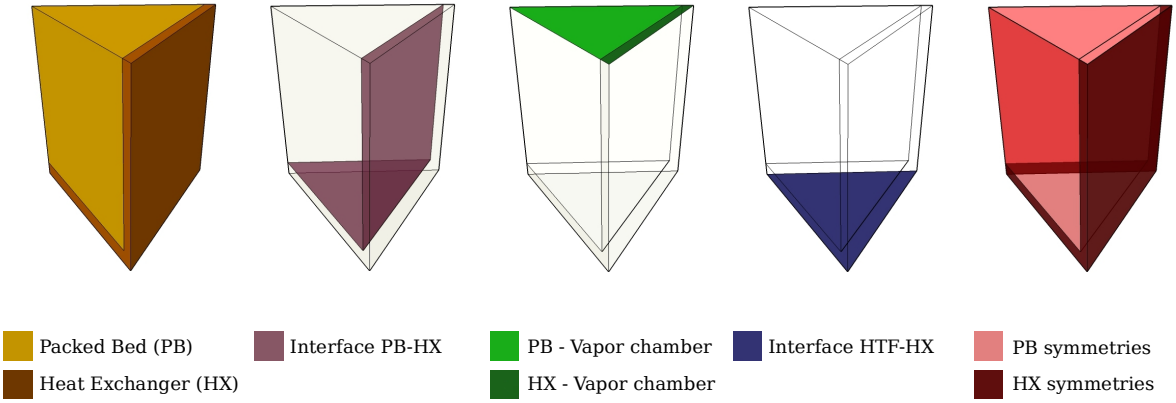

Figure 5: Boundary conditions of the computational domain

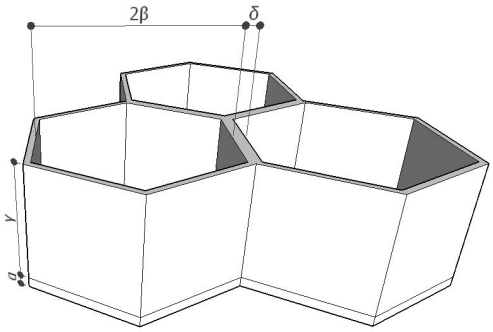

Figure 6: Dimensions of the geometry

4.4. Base scenario and studied range for the parametric study

For the parametric study, a base scenario is defined with respect to the geometrical and the operational parameters. Henceforth, each of these parameters is varied, in order to study its influence on the performance. Table 1 summarizes the parameters under investigation, their base scenario values, and the studied ranges.

Table 1: Base scenario values and studied range for the geometrical and operational parameters under investigation

Geometrical parameters		Base	Range	Unit
Cell inradius	β	3	1-6	mm
Cell height	γ	10	5-30	mm
Fin thickness	δ	1	0.5-3	mm
Operational parameters		**Base**	**Range**	**Unit**
Adsorption temperature	T_{ads}	30	20-40	°C
Desorption temperature	T_{des}	80	60-90	°C
Evaporator temperature	T_{eva}	10	5-15	°C
Condenser temperature	T_{con}	30	20-40	°C
Convection heat transfer coefficient	U_{HTF}	1000	600-2000	$\mathrm{Wm^{-2}K^{-1}}$
Cycle adsorption percentage (equation 19)	$\overline{w}_{\mathrm{rel}}$	70	50-90	%

Table 2 summarizes all the other input parameters of the model.

4.5. Graphs and contours interpretation

For each parameter under investigation, the reactor performance is reported in terms of the COP and SCP (Section 4.2). The cycle duration t_{cycle} is also reported, since it is adapted in each case. For sake of conciseness, the COP, the SCP and the t_{cycle} are reported in one graph. To achieve this, three vertical axes are incorporated. Each vertical axis is associated to its corresponding curve through the color (red for the SCP, blue for COP, green for t_{cycle}) and the symbol (circle for SCP, square for COP, triangle for t_{cycle}).

For the three geometric parameters, the spatial distribution of the adsorbed mass w_{rel} and the temperature are reported at 100 s after the beginning of the adsorption phase. The two-dimensional distributions pertain to the cross-section of the cell. Regarding the heat exchanger solid, w_{rel} does not apply, while temperature variations are visually imperceptible by the used scale, due to higher thermal conductivity.

5. Results and discussion

This section presents the results that arose from the simulations. The parameters under investigation are grouped in their respective sections, where the quantification of the reactor performance and the physical

Table 2: Model input parameters

Input parameter	Value	Unit	Ref.
$c_{p_{\mathrm{hx}}}$	385	$\mathrm{J\,kg^{-1}\,K^{-1}}$	[45]
$c_{p_{\mathrm{s,dry}}}$	924	$\mathrm{J\,kg^{-1}\,K^{-1}}$	[39]
d_{p}	0.0005	m	*
D_0	2.54×10^{-4}	$\mathrm{m^2\,s^{-1}}$	[11]
E_a	4.2×10^4	$\mathrm{J\,mol^{-1}}$	[11]
U_{if}	100	$\mathrm{W\,m^{-2}\,K^{-1}}$	[46]
K_0	7.3×10^{-13}	$\mathrm{kg_w\,kg_s\,Pa^{-1}}$	[39]
q_m	0.45	$\mathrm{kg_w\,kg_s^{-1}}$	[39]
ΔH_{ads}	2.693×10^6	$\mathrm{J\,kg^{-1}}$	[39]
ε_{b}	0.3955	-	[39][13]
ε_{p}	0.4287	-	[39][13]
ε_{t}	0.6546	-	[39][13]
ρ_{s}	2027	$\mathrm{kg\,m^{-3}}$	[39]
ρ_{hx}	8933	$\mathrm{kg\,m^{-3}}$	[45]
λ_{hx}	401	$\mathrm{W\,m^{-1}\,K^{-1}}$	[45]
λ_{s}	0.198	$\mathrm{W\,m^{-1}\,K^{-1}}$	[39]
τ	12	-	[39]

**Average particle diameter of the range provided by the manufacturer [38]*

phenomena involved are discussed. Subsequently, Section 5.5 elaborates the results from an engineering perspective, focusing on practical aspects of applications.

5.1. Geometrical parameters

Figure 7 presents the reactor performance results for cell inradius in the range of 1-6mm. Within the studied range, considerable variations are observed for both SCP and COP. On the one hand, the SCP decreases as the inradius increases, ranging between 80.4 W/kg and 218.9 W/kg for inradius of 6 and 1 mm, respectively. Lower inradius results in a more effective cooling of the packed bed. As observed in Figure 8, the temperature is maintained lower during adsorption, thus, the adsorbed mass is higher, leading to a higher rate of cooling production. On the other hand, the COP increases as the inradius increases, ranging between 0.356 and 0.606 for inradius of 1 and 6 mm, respectively. Lower inradius results in more densely packed cells, and thus, to a higher Solid Volume Fraction (SVF), the percentage of the heat exchanger solid volume with respect to the entire reactor volume. The SVF is 59.6% for $\beta = 1$ mm and 22.5% for $\beta = 6$ mm. As commented earlier, additional heat exchanger mass is associated to higher thermal input and thus, lower COP.

Figure 9 illustrates the reactor performance for cell height in the range of 5-30 mm. Within the studied

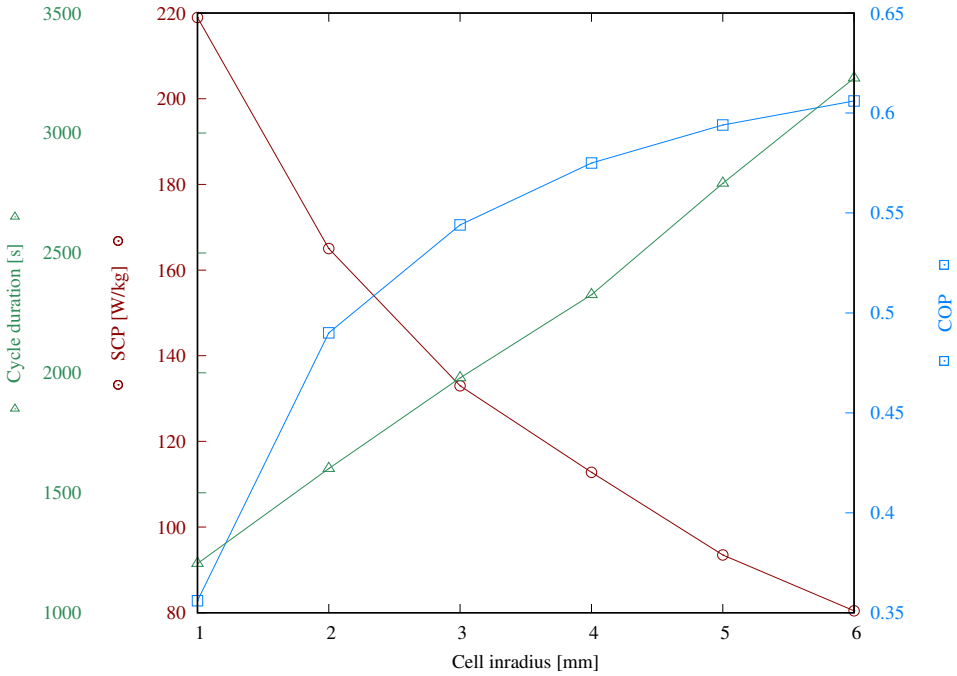

Figure 7: Reactor performance based on the cell inradius

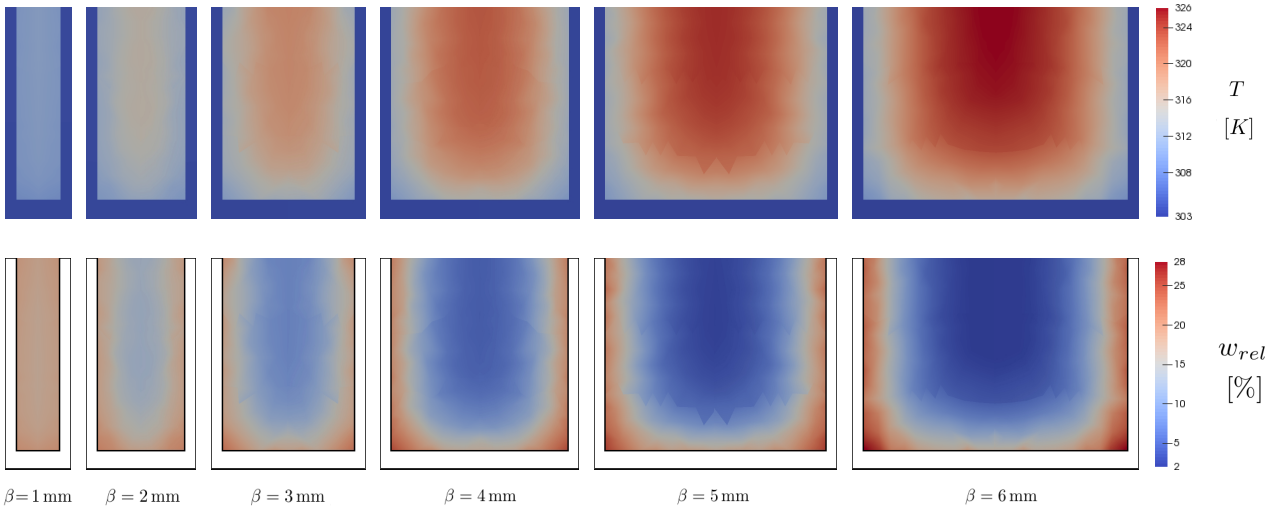

Figure 8: Spatial distribution of temperature (top) and relative adsorbed mass (bottom) at t=100s of adsorption phase for various cell inradii

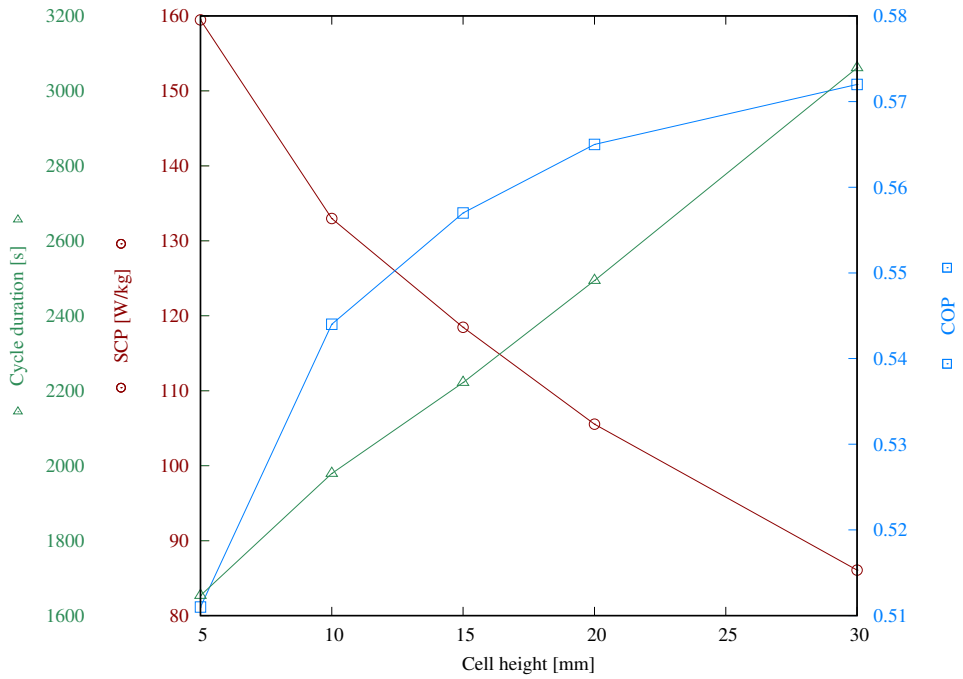

Figure 9: Reactor performance based on the cell height

range, the SCP halves approximately, though the COP does not experience such a drastic variation. The SCP decreases as the cell height increases, from 159.5 W/kg for $\gamma = 5$ mm to 86.1 W/kg for $\gamma = 30$ mm. As observed in Figure 10, the packed bed is cooled more effectively for lower cell height. For increasing cell heights, the released energy due to the exothermic nature of adsorption is removed less effectively, leading to higher temperatures and thus, lower adsorption capacity and cooling production. The COP increases from 0.51 for $\gamma = 5$ mm to 0.57 for $\gamma = 30$ mm. The COP variation is not so significant since the SVF does not vary considerably, being 38.3% for $\gamma = 5$ mm and 28.9% for $\gamma = 30$ mm.

Figure 11 shows the reactor performance for fin thickness in the range of 0.5-3 mm. The inverse effect is observed in comparison to the cell height case, namely, COP exhibits considerable variations, whereas SCP does not. In particular, SCP varies between 127.6 W/kg and 140.5 W/kg, corresponding to fin thickness of 0.5 and 3 mm, respectively. As observed in Figure 12, the temperature distribution of the packed bed is similar across the studied fin thicknesses. Consequently, the adsorption rate and the cooling production follow the same trend. However, at higher fin thicknesses the reactor is burdened with more heat exchanger solid, with the SVF being 22.5% and 59.6% for $\delta = 0.5$ mm and $\delta = 3$ mm, respectively. This considerable increase of the SVF results in a significant decrease of COP, from 0.599 for $\delta = 0.5$ mm to 0.364 for $\delta = 3$ mm.

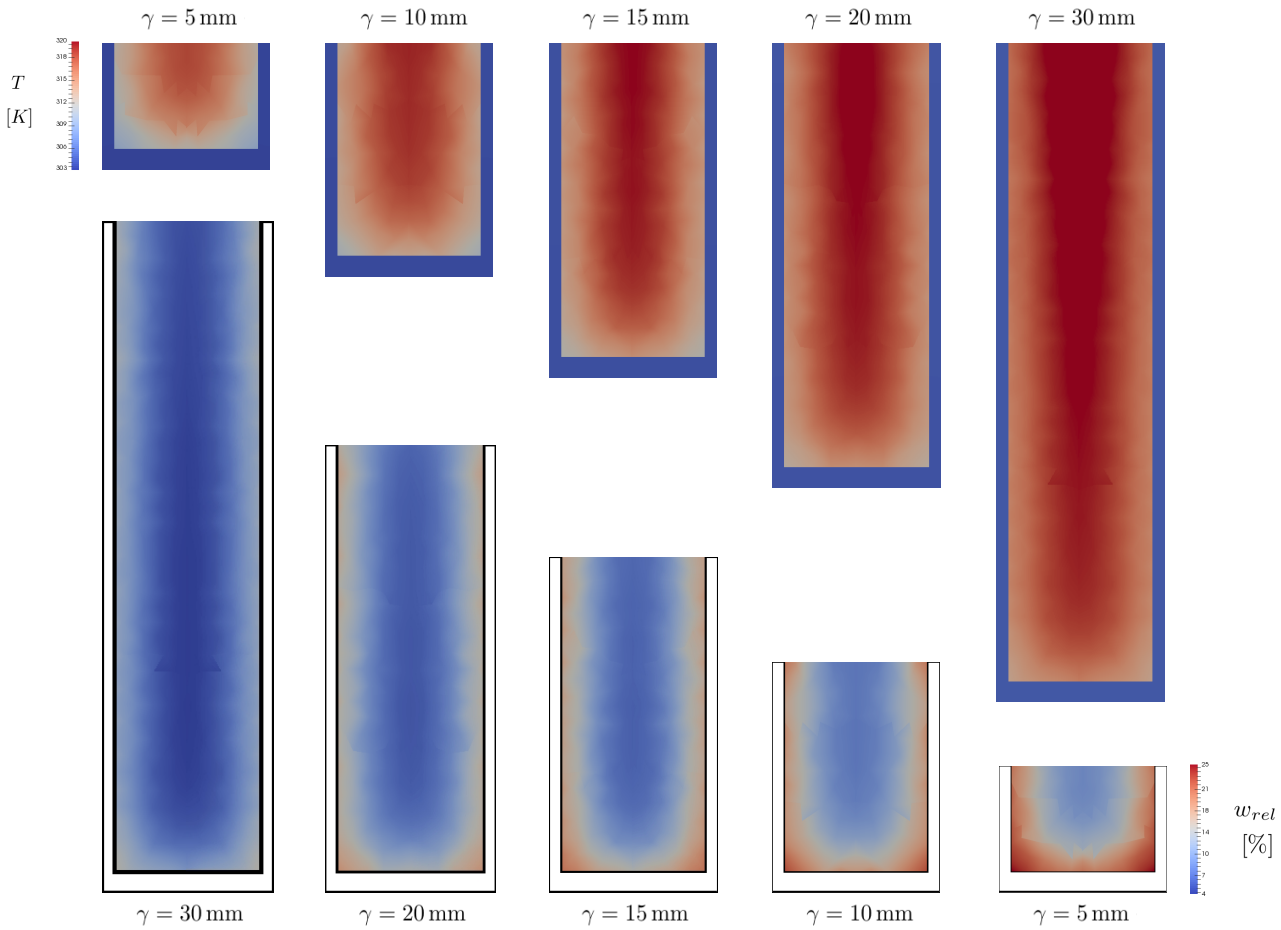

Figure 10: Spatial distribution of temperature (top) and relative adsorbed mass (bottom) at t=100s of adsorption phase for various cell heights

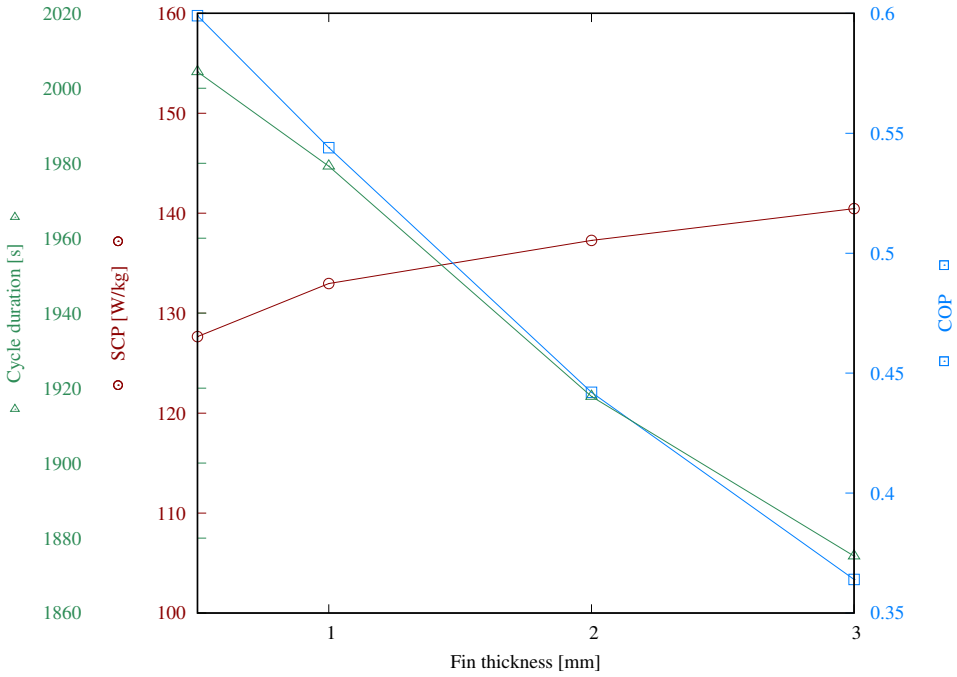

Figure 11: Reactor performance based on the fin thickness

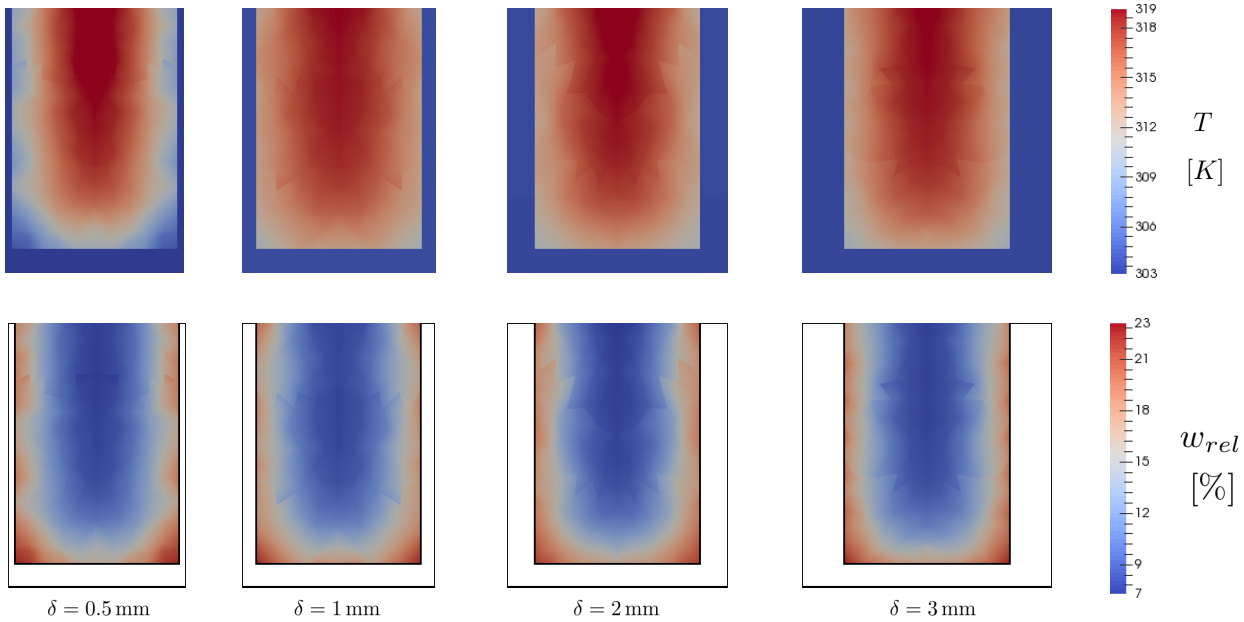

Figure 12: Spatial distribution of temperature (top) and relative adsorbed mass (bottom) at t=100s of adsorption phase for various fin thicknesses

5.2. Operating temperatures

This subsection elaborates the influence of the operating temperatures, namely, T_{des}, T_{ads}, T_{eva} and T_{con}. The latter two determine the P_{eva} and the P_{con}, respectively. Firstly, the quantitative results are presented graphically and the observed tendencies are commented briefly. Subsequently, a discussion is presented in order to facilitate the interpretation of the quantitative results. Through this discussion, it is attempted to provide an insight to the underlying physical phenomena involved.

Figure 13 illustrates the reactor performance based on the adsorption temperature T_{ads}, the HTF temperature during pre-cooling and adsorption. Both performance indicators decrease as the T_{ads} increases. The SCP decreases from 166.3 W/kg for $T_{\text{ads}} = 20\,^{\circ}\text{C}$ to 86.4 W/kg for $T_{\text{ads}} = 40\,^{\circ}\text{C}$. The COP decreases from 0.645 for $T_{\text{ads}} = 20\,^{\circ}\text{C}$ to 0.395 for $T_{\text{ads}} = 40\,^{\circ}\text{C}$. Figure 14 shows the reactor performance based on the desorption temperature T_{des}, the HTF temperature during pre-heating and desorption. The SCP is significantly influenced by the T_{des}, which almost triples within the range under consideration, from 53.6 W/kg for $T_{\text{des}} = 60\,^{\circ}\text{C}$ to 153.8 W/kg for $T_{\text{des}} = 90\,^{\circ}\text{C}$. Regarding the COP, it is observed that in the range 70-90 °C it is slightly affected by T_{des} – taking values between 0.531 and 0.544 – whereas at lower T_{des} it presents a sudden decrease until 0.47 for $T_{\text{des}} = 60\,^{\circ}\text{C}$. Although not plotted, the simulation was also performed for T_{des} of 52 °C and 55 °C. The corresponding SCP and COP are 25.3 W/kg and 0.356 for $T_{\text{des}} = 55\,^{\circ}\text{C}$, while for $T_{\text{des}} = 52\,^{\circ}\text{C}$, the SCP and COP are 6.6 W/kg y 0.154. The ability of the system to perform with so low driving temperature is an advantageous feature of adsorption cooling technology (discussed in Section 5.5).

Figure 15 illustrates the reactor performance as a function of the evaporator temperature T_{eva}. The reactor performance improves as the T_{eva} increases. In particular, the SCP increases from 95.4 W/kg for $T_{\text{eva}} = 5\,^{\circ}\text{C}$ to 168.8 W/kg for $T_{\text{eva}} = 15\,^{\circ}\text{C}$. The COP increases from 0.442 for $T_{\text{eva}} = 5\,^{\circ}\text{C}$ to 0.624 for $T_{\text{eva}} = 15\,^{\circ}\text{C}$. Figure 16 presents the results for the reactor performance based on the condenser temperature T_{con}. Both the SCP and the COP decrease as the T_{con} increases. The SCP decreases from 162.6 W/kg for $T_{\text{con}} = 20\,^{\circ}\text{C}$ to 93.1 W/kg for $T_{\text{con}} = 40\,^{\circ}\text{C}$, while the COP decreases from 0.588 for $T_{\text{con}} = 20\,^{\circ}\text{C}$ to 0.47 for $T_{\text{con}} = 40\,^{\circ}\text{C}$.

In order to gain insight to the underlying physical mechanisms, it is important to elaborate the impact of these parameters on the adsorption equilibrium, kinetics, heat transfer and thermodynamics involved.

Recalling equation 19, altering T_{des} or P_{con} alters the theoretical minimum adsorption equilibrium capacity of the cycle w^*_{min}. Similarly, altering T_{ads} or P_{eva} alters the theoretical maximum adsorption equilibrium capacity of the cycle w^*_{max}. Henceforth, the difference of the theoretical equilibrium capacities ($w^*_{\text{max}} - w^*_{\text{min}}$) is referred to as $\Delta w^*_{\text{cycle}}$. The $\Delta w^*_{\text{cycle}}$ influences both the adsorption equilibria and the adsorption kinetics. Regarding the equilibria, higher $\Delta w^*_{\text{cycle}}$ allows more vapor to be adsorbed per unit of mass of adsorbent in each cycle, thus the associated cooling produced Q_{cooling} is higher. This quantity is present in the numerator of both the SCP and the COP, hence, both performance indicators are benefited. Higher $\Delta w^*_{\text{cycle}}$ is achieved

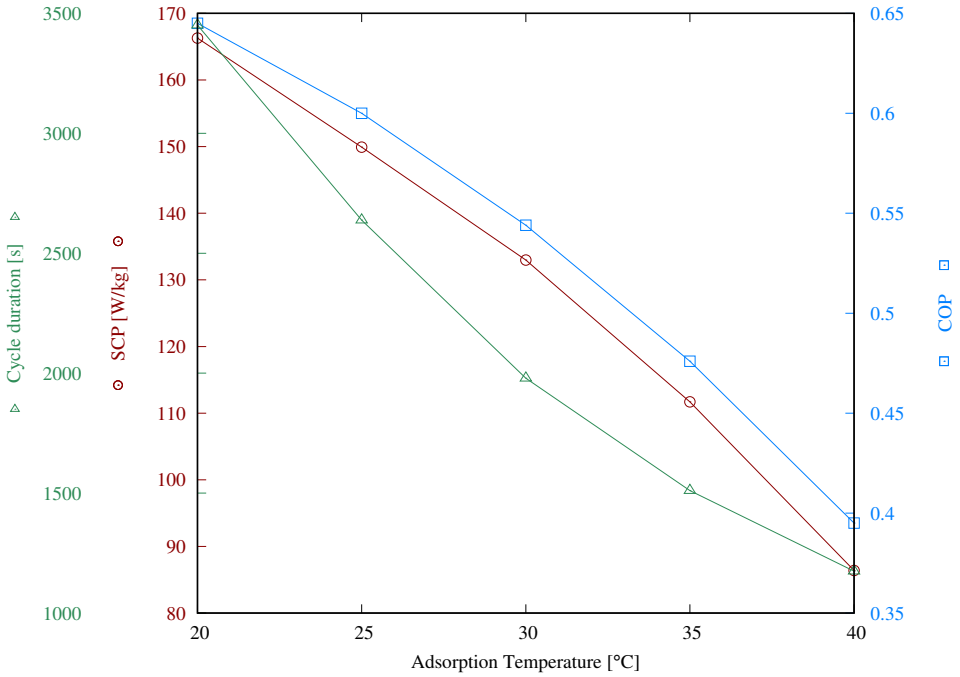

Figure 13: Reactor performance based on the adsorption temperature

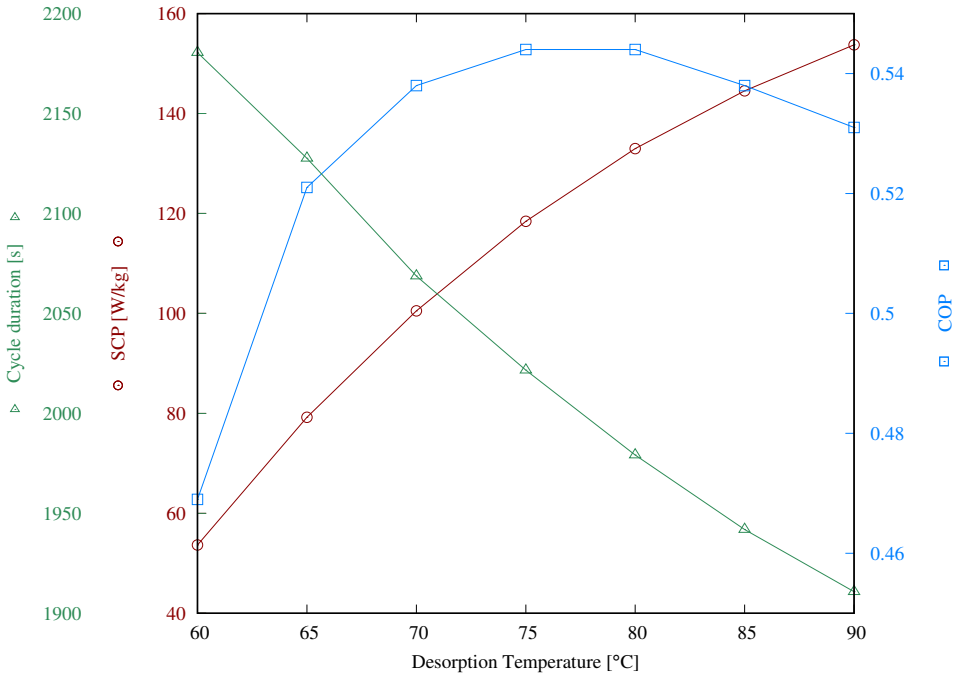

Figure 14: Reactor performance based on the desorption temperature

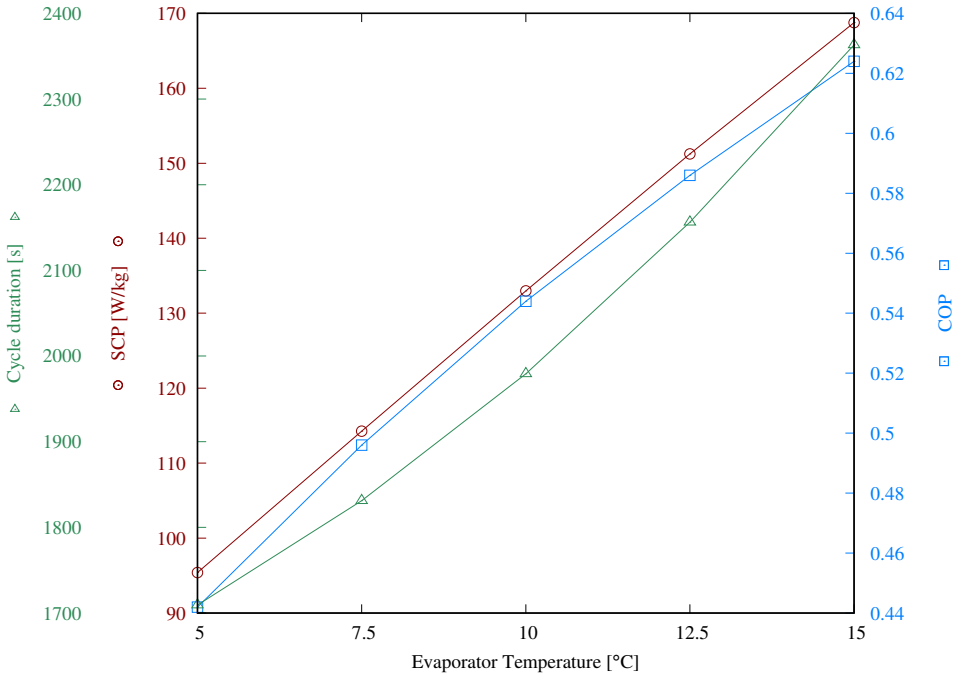

Figure 15: Reactor performance based on the evaporator temperature

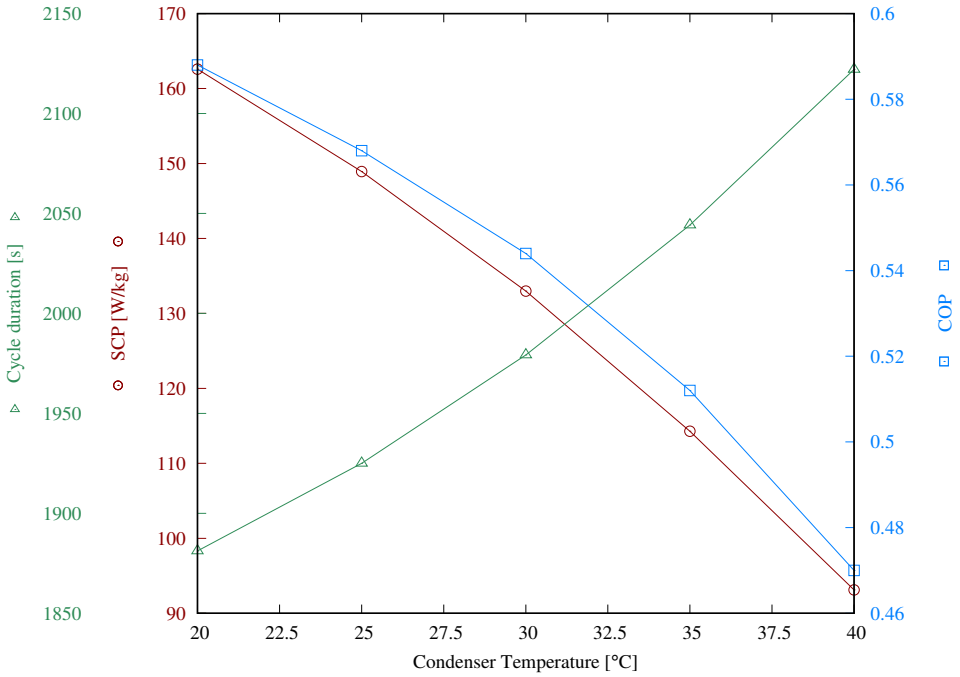

Figure 16: Reactor performance based on the condenser temperature

for lower T_{ads}, higher T_{des}, higher T_{eva}, and lower T_{con}. The influence of $\Delta w^*_{\mathrm{cycle}}$ on the adsorption kinetics is evident in equation 2. The adsorption rate is proportional to the difference $(w^* - w)$. Therefore, when $\Delta w^*_{\mathrm{cycle}}$ is higher, the rate of cooling production is higher as well, thus the SCP is benefited.

The adsorption kinetics are also influenced by the temperature dependence of the effective diffusivity, as expressed by the Arrhenius relation (equation 3). At higher temperature, the effective diffusivity increases, and thus, the sorption rate increases. With respect to T_{ads}, the effective diffusivity for $T_{\mathrm{ads}} = 40\,^{\circ}\mathrm{C}$ is approximately three times higher than for $T_{\mathrm{ads}} = 20\,^{\circ}\mathrm{C}$. However, the SCP still decreases, since the importance of decreasing $\Delta w^*_{\mathrm{cycle}}$ at higher T_{ads} is more prevalent. For the case of T_{des}, the effective diffusivity for $T_{\mathrm{des}} = 90\,^{\circ}\mathrm{C}$ is approximately 3.5 higher than for $T_{\mathrm{des}} = 60\,^{\circ}\mathrm{C}$. Higher desorption rate allows to desorb more effectively the water vapor and thus, to exploit at larger extent the $\Delta w^*_{\mathrm{cycle}}$.

Although a subtle influence, T_{eva} and T_{con} influence the thermodynamics of the system, as they alter the $\Delta H'_{\mathrm{evap}}$ (equation 23). The T_{eva} determines the enthalpy of the saturated vapor leaving the evaporator $h_{\mathrm{v,sat}}\big|_{T_{\mathrm{eva}}}$, while the T_{con} determines the enthalpy of the vapor-liquid mixture entering the evaporator $h_{\mathrm{l,sat}}\big|_{T_{\mathrm{con}}}$. At higher T_{eva} and lower T_{con}, the vapor adsorbed by the reactor is associated to higher cooling production. This effect is more notable for T_{con}, where the $\Delta H'_{\mathrm{evap}}$ for $T_{\mathrm{con}} = 20\,^{\circ}\mathrm{C}$ is 3.6% higher than for $T_{\mathrm{con}} = 40\,^{\circ}\mathrm{C}$, whereas the $\Delta H'_{\mathrm{evap}}$ for $T_{\mathrm{eva}} = 15\,^{\circ}\mathrm{C}$ is only 0.8% higher than for $T_{\mathrm{eva}} = 5\,^{\circ}\mathrm{C}$.

Apart from the influence of $\Delta w^*_{\mathrm{cycle}}$, the COP is also influenced by the actual values of w^*_{min} and w^*_{max}. To illustrate this, a simple example is employed, considering two cases A and B, with the same $\Delta w^*_{\mathrm{cycle}}$. The two cases are differentiated by the limits of $\Delta w^*_{\mathrm{cycle}}$, which are lower for case A; namely, $w^*_{\mathrm{min,A}} < w^*_{\mathrm{min,B}}$ and $w^*_{\mathrm{max,A}} < w^*_{\mathrm{max,B}}$. Although the cases have the same $\Delta w^*_{\mathrm{cycle}}$, case B would have lower COP. Part of the Q_{heating} – the thermal energy provided during pre-heating and desorption – is destined for the temperature increase of the reactor from T_{ads} to T_{des}. This amount of energy is higher for case B, since the thermal mass of the adsorbent is higher, due to its higher adsorbate content. In other words, at higher level of adsorbed mass, the energy required for desorption increases. Since the latter is the denominator of COP, this partially explains the sudden drop of COP for lower T_{des}.

5.3. Other operating parameters

The convection heat transfer coefficient U_{HTF} determines the heat transfer rate between the HTF and the heat exchanger solid. The U_{HTF} depends on the HTF properties, the channel geometry, the flow regime and the fluid velocity. Figure 17 shows the reactor performance as a function of the U_{HTF}. As observed, increasing the U_{HTF} results in a higher SCP. However, the benefit of increasing the U_{HTF} decreases at higher values. Within the range under consideration, the gradient of the SCP curve drops from 0.046 $(\mathrm{Wkg^{-1}})/(\mathrm{Wm^{-2}K})$ to 0.008 $(\mathrm{Wkg^{-1}})/(\mathrm{Wm^{-2}K})$, suggesting that further increasing the U_{HTF} is not beneficial. At higher

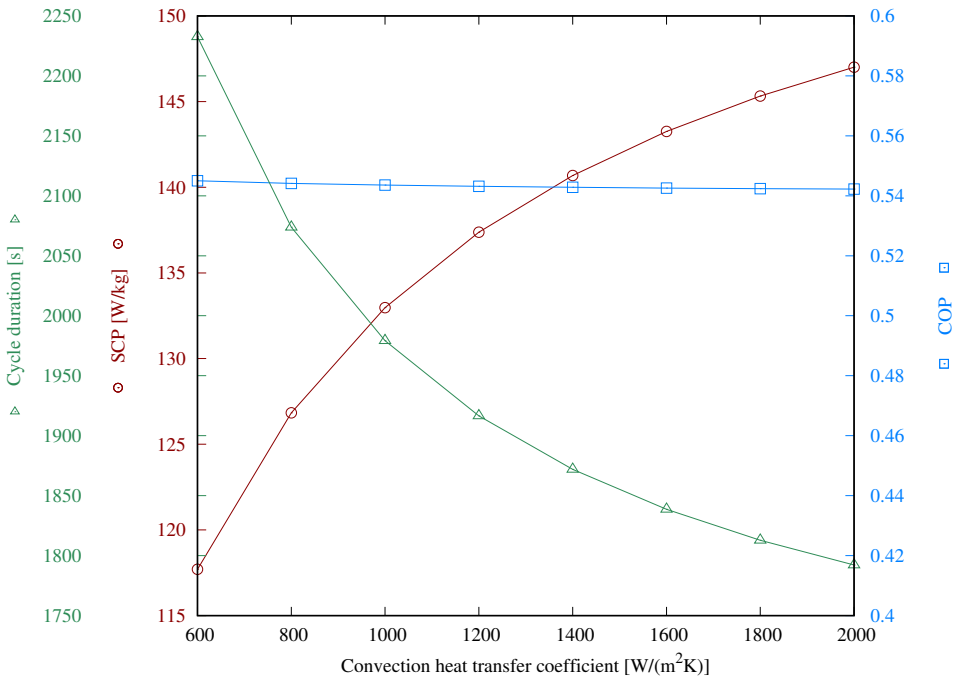

Figure 17: Reactor performance based on the convection heat transfer coefficient

U_{HTF}, the thermal resistance between the heat exchanger solid and the HTF decreases, and the cooling of the reactor is hindered mainly by the low heat transfer within the packed bed and the thermal resistance at its interface with the heat exchanger solid. Regarding the COP, the overall cooling produced and the thermal energy input do not vary significantly, leading to a fairly steady COP in the range under consideration.

The results presented so far followed the cycle duration scheme described in Section 4.1, using 70% as the cycle adsorption percentage $\overline{w}_{\mathrm{rel}}$. Figure 18 presents the influence of the $\overline{w}_{\mathrm{rel}}$. Recalling equation 2, the adsorption rate is proportional to the difference between the equilibrium capacity and the instantaneous adsorbed mass. Therefore, the adsorption rate is at its maximum at the beginning of the adsorption phase and it decreases as equilibrium is approached. Consequently, the SCP is higher when the adsorption phase is terminated earlier, namely, at lower cycle adsorption percentage. On the other hand, the required thermal input rate decreases at higher cycle time, since the temperature difference between the HTF and the reactor decreases. Prolonging the cycle time results in a higher COP, since the cooling energy produced during the adsorption phase - the COP numerator - increases at a higher rate than the thermal energy spent during pre-heating and desorption - the COP denominator. Within the studied range, the combination (COP, SCP) can be adjusted between (0.46, 165.1 $\mathrm{W/kg_s}$) for $t_{\mathrm{cycle}} = 1023\,\mathrm{s}$ and (0.59, 82.9 $\mathrm{W/kg_s}$) for $t_{\mathrm{cycle}} = 4122\,\mathrm{s}$.

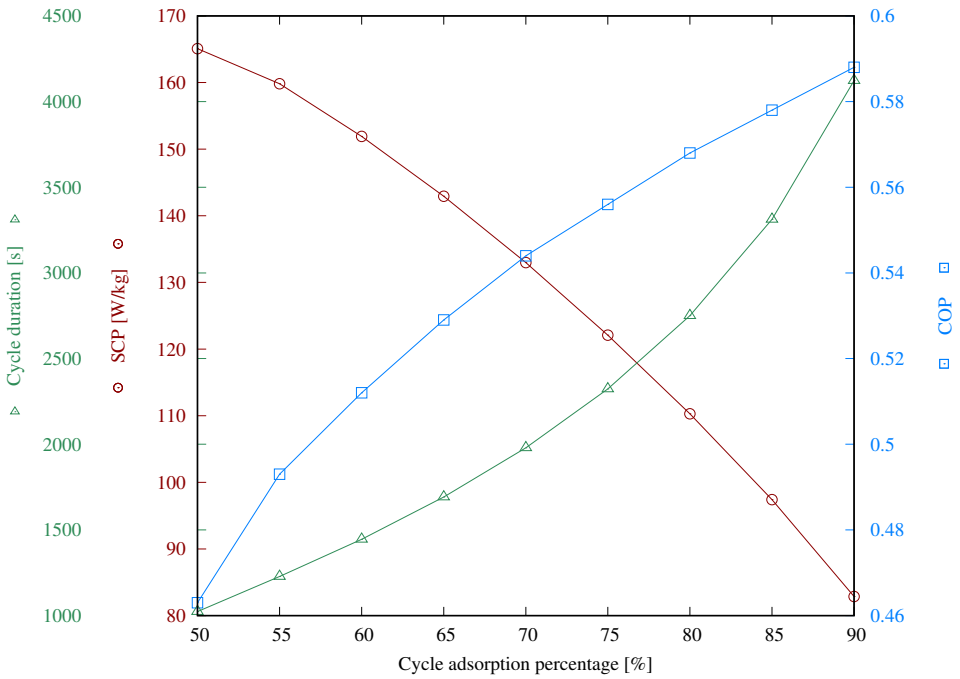

Figure 18: Reactor performance based on the cycle adsorption percentage

5.4. Heat exchanger material

In this section, copper and aluminium are compared as heat exchanger materials. The lower thermal conductivity of aluminium results in a slightly longer adsorption phase. The difference in the thermal mass of the two metals – $(\rho\, c_\mathrm{p})_\mathrm{Al} = 0.71 \times (\rho\, c_\mathrm{p})_\mathrm{Cu}$ – has two interesting effects. The lower thermal inertia of aluminium results in shorter pre-cooling and pre-heating time. It takes shorter period for the temperature change of the heat exchanger, thus, the pressure variation during the switching phases is achieved earlier. The latter compensates the slight increase of the adsorption phase, thus, the overall cycle duration decreases. Consequently, the SCP for aluminium is slightly higher (0.3%) than for copper.

Moreover, the COP for aluminium is higher than for the copper case, being 0.586 and 0.544 respectively. The energy input during pre-heating and desorption is distributed to (i) the increase of the heat exchanger solid temperature (ii) the temperature increase of the packed bed and (iii) the endothermic energy required for desorption. Orientative values are provided, normalized per kg of adsorbent for ease of comparison. The energy required for desorbing the adsorbate w_rel from 70% to 0% is 299 $\mathrm{kJ/kg_s}$. The energy required for increasing the adsorbent temperature by 50 °C is 72 $\mathrm{kJ/kg_s}$ (evaluating the thermal capacity of the wet adsorbent at the average adsorbed mass). Lastly, for this geometry, the energy required to increase 50 °C the heat exchanger solid is 122 $\mathrm{kJ/kg_s}$ for copper, whereas for aluminium is 87 $\mathrm{kJ/kg_s}$. This difference is reflected as a decrease in Q_heating and by consequence, as an increase of 7.7% in COP, for the case of aluminium.

5.5. Results discussion from engineering perspective

This section aims to provide an engineering perspective to the results. The reactor performance was characterized in terms of COP and SCP. As it arises, COP and SCP behave differently with respect to the variation of the studied parameters. It should be emphasized that, even though both indicators are significant, their importance is determined by the context of the application.

The SCP describes the cooling capacity per unit mass of adsorbent. Higher SCP is equivalent to less adsorbent material for a given capacity, as well as, more compact reactors. Thus, higher SCP is associated with lower initial investment for the adsorbent material and the reactor fabrication. Moreover, higher SCP is suitable for applications with space or weight constraints. Higher COP is equivalent to less thermal energy input for a given cooling capacity. Therefore, while SCP is associated to the initial investment, the COP is more related to the operating costs of the ACS. Furthermore, a higher COP corresponds to lower carbon emissions from the ACS operation, if carbon-positive energy sources are involved.

A COP-oriented application would be a solar-driven ACS located in a geographically isolated region, equipped with an auxiliary heater for periods with insufficient solar radiation. The inevitable consumption of the heater is inversely proportional to the COP. In such scenario, its fuel consumption can be associated to high cost and low availability. Therefore, a higher COP benefits the system by reducing the auxiliary consumption. An SCP-oriented application would be a vehicular cooling system driven by waste heat. The heat provided by the exhaust gases of the vehicle is not associated to any running costs. Thus, a lower COP is acceptable, in order to achieve a higher SCP, and hence, a compact and lightweight cooling system. As it arises from the results, the reactor geometry determines its performance, thus, its design should ensure a compromise between the SCP and COP, according to the particularities of each application.

The operating temperatures affect significantly the reactor performance. Low adsorption and condenser temperature benefit both the COP and the SCP. Thus, the heat rejection device (e.g. cooling tower) should be carefully designed, in order to cool effectively the HTF. Furthermore, the possibility of taking advantage of the outlet HTF from the condenser and adsorber should be considered. Exploiting this by-product of the ACS can reduce the consumption of the heat rejection device and one other application, such as: (i) pre-heating the domestic hot water in residential buildings or tourist facilities, (ii) in the latter, swimming pool heating and (iii) fuel pre-heating in vehicles or industry.

Even though the ACS performance declines at lower T_{des}, its operation in such conditions is advantageous in comparison to absorption cooling, which cannot utilize so low T_{des} [47, 48]. Thus ACSs are the only candidate for low temperature waste heat or solar collectors of lower efficiency and thus, lower cost. Moreover, this feature should be considered the control strategy. In a solar-driven application, a cloudy morning is associated with low T_{des}, but also, low cooling demand. If the capacity suffices to cover the load, the system

can operate without activating the auxiliary heater, reducing its energy consumption.

Attention should also be given in the heat transfer coefficient U_{HTF} between the HTF and the heat exchanger. On the one hand, a low value results in an additional thermal resistance and hinders the cooling of the reactor during adsorption. On the other hand, increasing excessively the U_{HTF} does not benefit further the performance and it might lead to unnecessarily high HTF pumping energy consumption.

The cycle duration has strong impact on the COP and SCP. Shorter cycles provide high SCP and low COP, whereas longer cycles provide the inverse. Consequently, cycle duration is identified as a useful manner to regulate the performance according to the instantaneous necessities. In a solar-cooled building, SCP can be prioritized during noon, when the cooling load and solar input peak – whereas during early morning, when the load is low but the solar input is insufficient and the auxiliary heater is used, COP can be prioritized in order to reduce the heater consumption.

With respect to the heat exchanger material, the lower thermal mass of aluminium results in a 7.7% higher COP in comparison to copper. A general suggestion is to employ materials with high thermal conductivity and low thermal mass ($\rho \times c_p$). Nevertheless, the choice of the material will be determined at large degree by technoeconomic criteria such as the material cost, as well as the cost and ease of fabrication.

6. Conclusions

Environmental benefits may arise from the widespread utilization of adsorption cooling systems. The design of the adsorption reactor – their core component – is a crucial task, since it determines its performance. A numerical investigation was conducted for the hexagonal honeycomb reactor – an underexplored geometry hitherto – using an in-house, validated model, based on three-dimensional unstructured meshes.

A parametric study was conducted for the dimensions that define the geometry, as well as for various operating parameters. The cell inradius creates a dichotomy between SCP and COP. The COP is 0.356 for $\beta = 1\,\mathrm{mm}$ and 0.606 for $\beta = 6\,\mathrm{mm}$, whereas the SCP is $218.9\,\mathrm{W/kg_s}$ for $\beta = 1\,\mathrm{mm}$ and $80.4\,\mathrm{W/kg_s}$ for $\beta = 6\,\mathrm{mm}$. Regarding the fin length, the SCP halves approximately in the studied range, being $159.5\,\mathrm{W/kg_s}$ for $\gamma = 5\,\mathrm{mm}$ and $86.1\,\mathrm{W/kg_s}$ for $\gamma = 30\,\mathrm{mm}$, whereas the COP is not significantly affected. The inverse effect is observed for the influence of the fin thickness. The impact of fin thickness on the COP is considerable, being 0.599 for $\delta = 0.5\,\mathrm{mm}$ and 0.364 for $\delta = 3\,\mathrm{mm}$, respectively, whereas the SCP is not significantly affected.

Regarding the operating temperatures, both performance indicators are maximized at the lowest adsorption and condenser temperature, as well as for the highest evaporator temperature. For the desorption temperature, the SCP exhibits its maximum at the highest value of the studied range, while for the COP, a

maximum is observed around 75-80 °C. The convection heat transfer coefficient does not affect the COP, but it influences the SCP considerably at the lower side of the range under consideration.

The cycle duration provokes a dichotomy between SCP and COP. Thus, it can be adjusted in order to adapt the performance to the instantaneous operating conditions, cooling demand and source availability. For the base scenario, the combination (COP, SCP) can be adjusted between (0.46, 165.1 W/kg_s) for $t_{cycle} = 1023$ s and (0.59, 82.9 W/kg_s) for $t_{cycle} = 4122$ s. Copper and aluminum were compared as heat exchanger materials. The COP for aluminium is 7.7% higher than for copper, due to its lower thermal mass. Finally, the results are discussed from an engineering perspective, elaborating practical aspects and applications.

At this stage, a reliable comparison with other reactor geometries found across the literature is not possible, since (i) distinct adsorption pairs are used, (ii) different operating conditions are considered, (iii) the employed models differ in terms of complexity or validation strictness and (iv) the reported results are not sufficient. Thus, a comparison might lead to unsafe conclusions about the geometries. Motivated by the low comparability, the next stage pertains to the simulation of several geometries with the same computational model and within the same framework, in order to extract reliable conclusions.

Acknowledgments

This study was financially supported by the Spanish Ministry of Economy, Industry and Competitiveness (MINECO, ENE2017-88697R).

References

[1] United Nations, Transforming our world: the 2030 Agenda for Sustainable Development (2015).

[2] R. Khosla, N. D. Miranda, P. A. Trotter, A. Mazzone, R. Renaldi, C. McElroy, F. Cohen, A. Jani, R. Perera-Salazar, M. McCulloch, Cooling for sustainable development, Nature Sustainability.doi:10.1038/s41893-020-00627-w.

[3] International Energy Agency, The Future of Cooling, IEA, Paris (2018).

[4] M. M. Younes, I. I. El-Sharkawy, A. Kabeel, B. B. Saha, A review on adsorbent-adsorbate pairs for cooling applications, Appl Therm Eng 114 (2017) 394 – 414. doi:10.1016/j.applthermaleng.2016.11.138.

[5] S. Yagnamurthy, D. Rakshit, S. Jain, B. B. Saha, Operational envelope and performance enhancement of a two-bed adsorption cooling system, Appl Therm Eng 195 (2021) 117181. doi:10.1016/j.applthermaleng.2021.117181.

[6] G. Papakokkinos, J. Castro, R. Capdevila, R. Damle, A comprehensive simulation tool for adsorption-based solar-cooled buildings – control strategy based on variable cycle duration, Energy and Buildings 231 (2021) 110591. doi:10.1016/j.enbuild.2020.110591.

[7] T. Nagel, S. Beckert, C. Lehmann, R. Gläser, O. Kolditz, Multi-physical continuum models of thermochemical heat storage and transformation in porous media and powder beds—a review, Appl Energy 178 (2016) 323 – 345. doi:10.1016/j.apenergy.2016.06.051.

[8] G. Papakokkinos, Computational modeling of adsorption packed bed reactors and solar-driven adsorption cooling systems, Ph.D. thesis, Universitat Politècnica de Catalunya, www.tdx.cat/handle/10803/672099 (2021).

[9] M. Chahbani, J. Labidi, J. Paris, Effect of mass transfer kinetics on the performance of adsorptive heat pump systems, Appl Therm Eng 22 (1) (2002) 23 – 40. doi:10.1016/S1359-4311(01)00067-9.

[10] E. Pérez, I. Romero, A. Albis, M. Carmona, Modeling and experiments on a finned cylindrical reactor with expanded graphite/activated carbon/lithium chloride-ammonia for chemisorption refrigeration systems, Appl Therm Eng 184 (2021) 116281. doi:10.1016/j.applthermaleng.2020.116281.

[11] B. B. Saha, A. Chakraborty, S. Koyama, Y. I. Aristov, A new generation cooling device employing $CaCl_2$-in-silica gel–water system, Int J Heat Mass Transf 52 (1) (2009) 516 – 524. doi:10.1016/j.ijheatmasstransfer.2008.06.018.

[12] Q. Pan, R. Wang, L. Wang, Comparison of different kinds of heat recoveries applied in adsorption refrigeration system, Int J Refrig 55 (2015) 37 – 48. doi:10.1016/j.ijrefrig.2015.03.022.

[13] G. Papakokkinos, J. Castro, J. López, A. Oliva, A generalized computational model for the simulation of adsorption packed bed reactors – parametric study of five reactor geometries for cooling applications, Appl Energy 235 (2019) 409 – 427. doi:10.1016/j.apenergy.2018.10.081.

[14] İsmail Solmuş, C. Yamali, C. Yildirim, K. Bilen, Transient behavior of a cylindrical adsorbent bed during the adsorption process, Appl Energy 142 (2015) 115 – 124. doi:10.1016/j.apenergy.2014.12.080.

[15] Y. Liu, K. Leong, The effect of operating conditions on the performance of zeolite/water adsorption cooling systems, Appl Therm Eng 25 (10) (2005) 1403 – 1418. doi:10.1016/j.applthermaleng.2004.09.013.

[16] H. Niazmand, I. Dabzadeh, Numerical simulation of heat and mass transfer in adsorbent beds with annular fins, Int J Refrig 35 (3) (2012) 581 – 593. doi:10.1016/j.ijrefrig.2011.05.013.

[17] S. Hong, S. Ahn, O. Kwon, J. Chung, Optimization of a fin-tube type adsorption chiller by design of experiment, Int J Refrig 49 (2015) 49 – 56. doi:10.1016/j.ijrefrig.2014.09.022.

[18] M. Khanam, S. Jribi, T. Miyazaki, B. Saha, S. Koyama, Numerical investigation of small-scale adsorption cooling system performance employing activated carbon-ethanol pair, Energies 11 (6). doi:10.3390/en11061499.

[19] M. Elsheniti, M. keywords =, Examination of effects of operating and geometric parameters on the performance of a two-bed adsorption chiller, Appl Therm Eng 146 (2019) 674 – 687. doi:10.1016/j.applthermaleng.2018.10.043.

[20] S. Mitra, M. Muttakin, K. Thu, B. B. Saha, Study on the influence of adsorbent particle size and heat exchanger aspect ratio on dynamic adsorption characteristics, Appl Therm Eng 133 (2018) 764 – 773. doi:10.1016/j.applthermaleng.2018.01.015.

[21] I. Albaik, R. Al-Dadah, S. Mahmoud, İsmail Solmaz, Non-equilibrium numerical modelling of finned tube heat exchanger for adsorption desalination/cooling system using segregated solution approach, Appl Therm Eng 183 (2021) 116171. doi:10.1016/j.applthermaleng.2020.116171.

[22] B. Golparvar, H. Niazmand, A. Sharafian, A. A. Hosseini, Optimum fin spacing of finned tube adsorber bed heat exchangers in an exhaust gas-driven adsorption cooling system, Appl Energy 232 (2018) 504 – 516. doi:10.1016/j.apenergy.2018.10.002.

[23] M. Mahdavikhah, H. Niazmand, Effects of plate finned heat exchanger parameters on the adsorption chiller performance, Appl Therm Eng 50 (1) (2013) 939 – 949. doi:10.1016/j.applthermaleng.2012.08.033.

[24] H. R. Ramji, S. L. Leo, M. O. Abdullah, Parametric study and simulation of a heat-driven adsorber for air conditioning system employing activated carbon–methanol working pair, Appl Energy 113 (2014) 324 – 333. doi:10.1016/j.apenergy.2013.07.017.

[25] R. H. Mohammed, O. Mesalhy, M. L. Elsayed, L. C. Chow, Novel compact bed design for adsorption cooling systems: Parametric numerical study, Int J Refrig 80 (2017) 238 – 251. doi:10.1016/j.ijrefrig.2017.04.028.

[26] R. H. Mohammed, O. Mesalhy, M. L. Elsayed, L. C. Chow, Performance evaluation of a new modular packed bed for adsorption cooling systems, Appl Therm Eng 136 (2018) 293 – 300. doi:10.1016/j.applthermaleng.2018.02.103.

[27] M. M. Saleh, R. Al-Dadah, S. Mahmoud, E. Elsayed, O. El-Samni, Wire fin heat exchanger using aluminium fumarate for

adsorption heat pumps, Appl Therm Eng 164 (2020) 114426. doi:10.1016/j.applthermaleng.2019.114426.

[28] M. M. Kowsari, H. Niazmand, M. M. Tokarev, Bed configuration effects on the finned flat-tube adsorption heat exchanger performance: Numerical modeling and experimental validation, Appl Energy 213 (2018) 540 – 554. doi:10.1016/j.apenergy.2017.11.019.

[29] M. Khatibi, M. Mohammadzadeh Kowsari, B. Golparvar, H. Niazmand, Optimum loading of aluminum additive particles in unconsolidated beds of finned flat-tube heat exchangers in an adsorption cooling system, Appl Therm Eng 196 (2021) 117267. doi:10.1016/j.applthermaleng.2021.117267.

[30] Q. Zhang, X. Yang, P. Li, G. Huang, S. Feng, C. Shen, B. Han, X. Zhang, F. Jin, F. Xu, T. J. Lu, Bioinspired engineering of honeycomb structure – using nature to inspire human innovation, Prog. Mater. Sci 74 (2015) 332 – 400. doi:10.1016/j.pmatsci.2015.05.001.

[31] T. Hales, The honeycomb conjecture, Discrete Comput Geom 25 (2001) 1 – 22. doi:10.1007/s004540010071.

[32] H. Zhang, X. Liu, H. Hong, H. Jin, Characteristics of a 10 kW honeycomb reactor for natural gas fueled chemical-looping combustion, Appl Energy 213 (2018) 285–292. doi:10.1016/j.apenergy.2018.01.037.

[33] C. Corgnale, B. Hardy, R. Chahine, D. Cossement, Hydrogen desorption using honeycomb finned heat exchangers integrated in adsorbent storage systems, Appl Energy 213 (2018) 426 – 434. doi:10.1016/j.apenergy.2018.01.003.

[34] M. Bilardo, G. Fraisse, M. Pailha, E. Fabrizio, Design and experimental analysis of an integral collector storage (ICS) prototype for DHW production, Appl Energy 259 (2020) 114104. doi:10.1016/j.apenergy.2019.114104.

[35] B. Shi, A. Elsayed, R. AL-Dadah, S. Mahmoud, CFD simulation of honeycomb adsorption bed for automotive cooling system, In Proceedings of the International Conference on Heat Transfer and Fluid Flow, Prague, Czech Republic, 2014.

[36] M. Sosnowski, J. Krzywanski, K. Grabowska, M. Makowska-Janusik, W. Nowak, K. Sztekker, A. Yousef, Implementation of honeycomb bed in an adsorption cooling technology, In Proceedings of ECOS 2019, The 32th International Conference on efficiency, cost, optimization, simulation and environmental impact of energy systems, June 23-28, Wroclaw, Poland.

[37] A. D. Nield, A. Bejan, Convection in Porous Media, 4th Edition, Springer-Verlag New York, 2013.

[38] Fuji Silysia Chemical LTD. (Nagoya, Japan).

[39] X. Wang, W. Zimmermann, K. C. Ng, A. Chakraboty, J. U. Keller, Investigation on the isotherm of silica gel+water systems, J Therm Anal Cal 76 (2) (2004) 659 – 669. doi:10.1023/B:JTAN.0000028045.96239.7e.

[40] M. Suzuki, Adsorption Engineering, Kodansha, Tokyo and Elsevier Science Publishers, Amsterdam, 1990.

[41] N. Wakao, S. Kaguei, Heat and Mass Transfer in Packed Beds, 1st Edition, Gordon and Breach Science Publishers, 1982.

[42] W. Wagner, H. J. Kretzschmar, International Steam Tables - Properties of Water and Steam based on the Industrial Formulation IAPWS-IF97, 2nd Edition, Springer-Verlag Berlin Heidelberg, 2008.

[43] L. Sun, N. B. Amar, F. Meunier, Numerical study on coupled heat and mass transfers in an absorber with external fluid heating, Heat Recov Syst CHP 15 (1) (1995) 19 – 29. doi:10.1016/0890-4332(95)90034-9.

[44] S. Jribi, T. Miyazaki, B. B. Saha, S. Koyama, S. Maeda, T. Maruyama, CFD simulation and experimental validation of ethanol adsorption onto activated carbon packed heat exchanger, Int J Refrig 74 (2017) 345 – 353. doi:10.1016/j.ijrefrig.2016.10.019.

[45] T. Bergman, A. Lavine, F. Incropera, D. DeWitt, Fundamentals of Heat and Mass Transfer, 7th Edition, John Wiley and Sons, 2011.

[46] I. Glaznev, Y. Aristov, The effect of cycle boundary conditions and adsorbent grain size on the water sorption dynamics in adsorption chillers, Int J Heat Mass Transf 53 (9) (2010) 1893 – 1898. doi:10.1016/j.ijheatmasstransfer.2009.12.069.

[47] R. Wang, L. Wang, W. J, Adsorption Refrigeration Technology, 1st Edition, John Wiley and Sons, 2014.

[48] S. Ajib, A. Alahmer, Solar Cooling Technologies, in: I. H. Al-Bahadly (Ed.), Energy Conversion - Current Technologies and Future Trends, Chapters, IntechOpen, 2019. doi:10.5772/intechopen.80484.